# On gas bubbles in industrial aluminium cells with prebaked anodes and their influence on the current distribution

J. ZORIC and A. SOLHEIM
*SINTEF Materials Technology, N-7465 Trondheim, Norway*

## Abstract

The secondary current distribution in industrial aluminium cells with prebaked anodes was calculated, taking into account the gas bubbles. The input data were obtained on the basis of a physical model and data suggested in the literature. The bubbles were modelled in the following manner: (i) as very small bubbles dispersed in a homogeneous layer with higher electrical resistivity than the bulk of the electrolyte, (ii) as large bubbles modelled as discrete slabs with infinite resistivity, and (iii) as a combination of (i) and (ii). The bubble size and the number of bubbles, as well as the resistance of the homogeneous bubble layer, were varied to give an equivalent voltage drop in the range 0.1–0.4 V. Large bubbles (slabs) appeared to have a significant screening effect on the anodic current densities. The anodic current densities between slabs showed local maxima, sometimes reaching twice the value of the working current density (0.75 A cm$^{-2}$). The cathodic current densities had local minima underneath the large anodic bubbles, following their position at the anode. Underneath a bubble of 6.1 cm width, the cathodic current density decreased from 0.75 to 0.23 A cm$^{-2}$.

## List of symbols

$F$    faradaic constant (96 487 As mol$^{-1}$)
$h'$    average amount of gas between gas slabs
$j$    current density (A cm$^{-2}$)
$L$    horizontal distance (m)
$P$    pressure (Pa)
$q$    volumetric rate of gas formation (m$^3$ s$^{-1}$ m$^{-2}$)
$R$    universal gas constant (8.3143 J mol$^{-1}$ K$^{-1}$)
$T$    temperature (K)
$t$    time (s)
$u$    slab velocity (m s$^{-1}$)
$x$    distance from the trailing edge of the leading gas slab

*Greek letters*
$\delta$    thickness of bubble layer (m)
$\eta$    overvoltage (V)
$\varphi$    surface coverage
$\rho$    resistivity ($\Omega$ cm)
$\Delta U$    extra voltage drop due to bubbles (V)
$v$    slab velocity

*Subscripts*
0    bubble-free
A    anode
b    bubble, bubble layer
C    cathode
CC    centre–centre

## 1. Introduction

Primary aluminium is produced in electrolysis cells with horizontal carbon anodes and the liquid aluminium pool acting as a cathode. The primary cell reaction can be written as

$$Al_2O_3 + \frac{3}{2}C = 2\,Al + \frac{3}{2}CO_2 \tag{1}$$
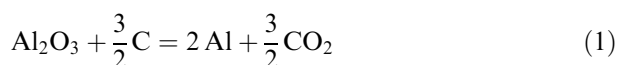
The anode is consumed at a rate of about 1.5 cm per day, so the anode must be renewed either by removing butts and setting a new anode block (prebake technology), or by semicontinuous feeding of 'green' anode mass (self-baking anode, Søderberg technology). Most of the current passes between the cathode and the horizontal part of the anode facing the cathode, but some current also flows through the vertical sides of the anode. The rate of gas evolution at the underside of the anode is fairly high (about 0.002 m$^3$ s$^{-1}$ m$^{-2}$). Obviously, the total cell resistance, as well as the local current distribution, must be influenced by the presence of gas bubbles. According to Haupin [1], the extra ohmic drop in the electrolyte due to the presence of gas bubbles may be in the range of 0.15–0.35 V.

Immediately upon setting, a new cold anode block (the surface of the horizontal section is typically 1 m$^2$), becomes covered with a layer of frozen electrolyte which slowly melt away during 12–18 h [2]. Apparently, the sides and the corners of the anode block first get exposed to molten bath and start to draw current, while the

central part of the underside gets exposed several hours later. The initially sharp corners get rounded off due to the higher current density in that region (in 3–8 days, depending on the geometry of the cell and also the initial shape of the anode. The lifetime of the anode is 3–4 weeks). These effects are probably important in facilitating the escape of gas from the underside of the anode. However, model experiments have shown that inclinations as small as 0.3° are sufficient to set bubbles in motion [3, 4].

In our earlier modelling work [5–8], the current distribution and steady state anode shapes in cells with prebaked and Søderberg anodes were studied. In that work, and also in much of the previous literature, it was assumed that the electrolyte has a uniform electrical conductivity. In reality, regions containing a mixture of electrolyte and gas bubbles have a lower conductivity than the gas-free electrolyte.

The main idea of the present work was to study to which extent the local current densities are influenced by the presence of gas bubbles, by means of mathematical modelling of the secondary current distribution (taking into account the anodic and cathodic overvoltages). Existing hypotheses and assumptions about bubbles originating from physical modelling, various industrial measurements, and visual observations (presented in Table 1), were used as the input data. The motivation to understand the current distribution is very practical, since the ohmic voltage drop in the electrolyte represents almost 40% of the total electrical energy input to the cell, or 67% of the net heat generated [9–12].

## 2. Geometry of the gas bubble layer

Although the literature on formation, growth, and motion of gas bubbles in aqueous solutions is huge, relatively little is known about behaviour of bubbles formed in melts or underneath nearly horizontal surfaces. The authors have not found published data concerning mathematical modelling of the secondary current distribution in industrial aluminium cells that include modelling of gas bubbles. The most probable reason is that the knowledge about the bubbles is fairly limited. The bubble coverage on the anodes, which must be assumed to vary during industrial operation, is not known. In spite of that, the effect of gas bubbles are incorporated in some analyses, such as the so-called fanning factors derived by Haupin [1] and description of current pickup upon setting of new anodes [13].

A number of mathematical models have been developed, considering the effect of gas bubbles from a rather

*Table 1.* Estimated parameters concerning gas induced bubbles in industrial aluminium cells founded in references

PM – data obtained by physical modelling

M – data obtained by measurements in industrial cells

| Value | Reference | Method | Comments |
|---|---|---|---|
| **Thickness of the bubble layer/cm** | | | |
| 0.4–0.6 | Aaberg [19] | PM | Range up to 0.71 cm |
| 0.5 | Fortin [3] | PM | |
| 0.5 | Haupin [1, 18] | M | Occasional contact  between the probe and the gas bubbles observed as far as 2 cm |
| 0.5 | Dewing [25] | PM | |
| 0.4 | Oye [26] | PM | |
| 0.2–0.3 | Begunov [27–29] | PM | |
| **Shape and dimensions of the bubbles – the bubble profile** | | | |
| | Fortin [3] | PM | Large bubbles; bubble front thickness 0.8–2.4 cm, longitudinal dimension of the bubbles 2–128 cm at the centre of the anode, transverse dimension varied 4–40 cm |
| | Begunov [27–29] | PM | Dimensions of the gas bubbles fluctuate within fairly wide limits, from spherical bubbles about 0.2 cm dia. to films extending 1–1.2 cm or more |
| **Average gas bubble coverage** | | | |
| 0.5–0.6 | Fortin [3] | PM | Values vary from 0.24 up to 0.9 |
| 0.65–0.90 | Aaberg [19] | PM | |
| 0.5 | Dewing [25] | PM | |
| **Bubble layer voltage drop/V** | | | |
| 0.15–0.35 | Haupin [1] | M | |
| 0.24–0.45 | Solheim [17] | PM | |
| **Average gas volume/cm$^3$ cm$^{-2}$** | | | |
| 0.4–0.6 | Aaberg [19] | PM | |
| 0.2–0.5 | Houston [9] | PM | |
| 0.3–0.6 | Siraev [20] | PM | |
| **Frequency of gas bubble release/Hz** | | | |
| 0.2–3.3 | Fortin [3] | PM | |
| 0.2–2 | Begunov [27] | PM | |
| 0.5–1 | Present work | M | Observations in industrial cells |

global standpoint (i.e., the impact of gas induced bubbles on the hydrodynamics of the cell, the resistivity of the electrolyte etc.) [14–16]. Still, the main sources of knowledge about gas bubbles in aluminium cells appear to be the measurements in physical models.

In electrolysis cells, bubbles initially grow by diffusion of gas from the supersaturated liquid along the perimeter of the bubble. In low-temperature models, however, gas evolution is simulated by passing gas through a porous medium. Such bubbles grow by gas entering directly into the bubble, which possibly favours the formation of larger bubbles. However, this difference is not necessarily important, since it is likely that coalescence is the main mechanism for bubble growth. Small bubbles forming on the anode surface do not significantly affect the motion of large bubbles, as confirmed by Thonstad and Ngoya [4]. In the following account, we will focus mainly on works that can suggest input values about the geometry of the bubble layer.

Fortin et al. [3] used a full-scale model shaped as a 2D transverse section through a 150 kA prebake aluminium cell (similar to the cell we are treating in this work). Anodic gas evolution was simulated by passing air through a porous polyethylene plate. A tilt of a fraction of a degree was sufficient to induce significant buoyancy driven motion of the gas bubbles. Generally, the bubbles produced were large, and the main mechanism of growth was by coalescence. The longitudinal dimension varied from 2 to 128 cm, and the dimension perpendicular to the direction of motion was 4–40 cm (the entire width of the anode slice). The bubbles had a thick front (0.8–2.4 cm) and a thinner trailing portion (about 0.5 cm). About 24–90% of the anode was covered by gas, depending on the current density, the liquid velocity, and the angle of inclination. The bubble release frequency was 0.2–3.3 bubbles per second. Solheim and Thonstad made similar visual observations in their physical model [17]. It appeared that the transversal dimension of large bubbles was larger than the longitudinal dimension.

Similar bubble shapes and dimensions were found in connection with the present work, using a tank containing water and a slanted 'anode' (this device was not intended as a geometrically and dynamically correct physical model of an industrial cell). Some of the pictures, recorded by video, are shown in Figures 1 and 2. As shown in Figure 1, the bubble size depends on the angle of inclination. The larger bubbles (7–12 cm) have developed the typical 'head and tail' shape. Smaller bubbles (1–3 cm length) have elliptical shape and they are positioned between the larger bubbles. A view from the bottom side of the cell is shown in Figure 2. It can be observed that bubbles cover a significant fraction of the anode underside, and that the bubbles have the largest dimensions transversal to the travelling direction. These observations agree well with Fortin [3].

Haupin [1, 18] measured the bubble layer voltage drop *in situ* by moving a reference electrode from the cathode towards the anode. He obtained values of 0.15–0.35 V at
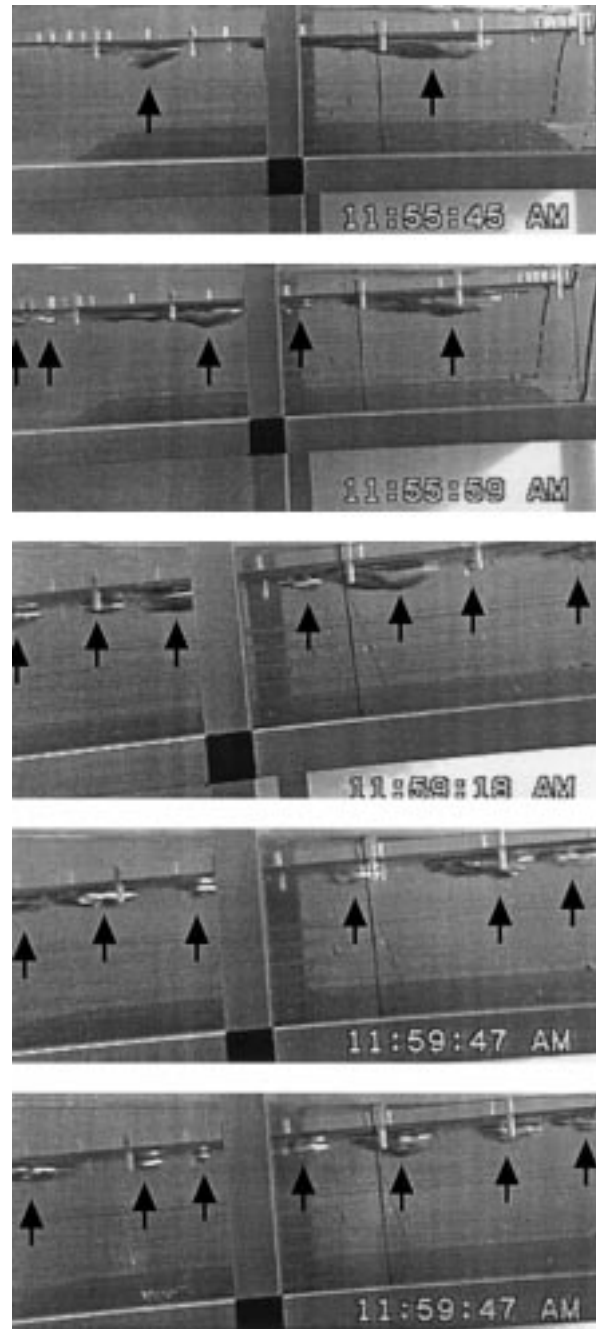


*Fig. 1.* Bubbles of air in water, travelling underneath an 'anode'. Larger bubbles shown in the two upper pictures have developed the typical 'head and trail' shape. Smaller bubbles (in the two lower pictures) have elliptical shape when viewed from the underside. Supporting aluminium tubes in the foreground are 2.5 cm × 2.5 cm square.

an anodic current density of 0.8 A cm$^{-2}$. In those experiments, the electrical signal became very noisy as the voltage probe entered the gas bubble layer, approximately 5 mm from the anode face. Occasional contact between the probe and the gas bubbles was detected as far as 2 cm from the anode face.

Solheim and Thonstad [17] measured the amount of gas accumulated under the anode as well as the 'bath' resistance in a room temperature water model. The bubble size was varied by addition of small amounts of
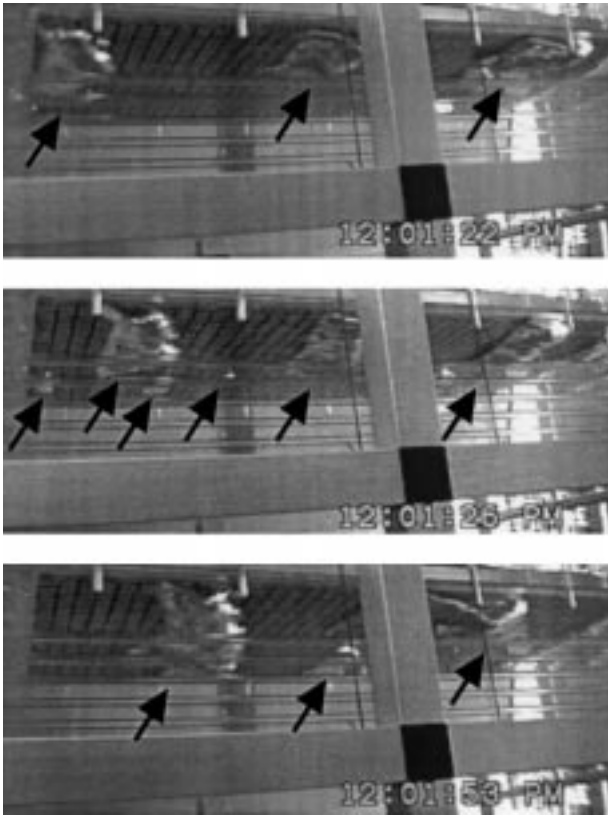
*Fig. 2.* Bubbles of air in water travelling underneath an 'anode'; view from underside. As can be observed, the largest dimension is transversal to the direction of motion. Mesh on the 'anode' (barely visible) is 1 cm × 1 cm, and the supporting aluminium tubes are 2.5 cm × 2.5 cm square.

1-propanol to the water, which inhibited coalescence. It was found that decreasing bubble size gave larger amounts of accumulated gas, as well as higher resistivity in the bubble layer. The gas-induced extra resistance varied more than one order of magnitude, all other factors than the bubble size being constant, and only the largest bubbles (water without 1-propanol) gave realistic values of the gas-induced voltage drop when recalculated for an industrial prebaked anode (0.24–0.45 V). In that case, the amount of accumulated gas was 0.16–0.28 $cm^3$ gas ($cm^2$ anode surface area)$^{-1}$ which is somewhat lower than indicated in most of the work considering volume of accumulated gas, for example, Aaberg [19], Houston [9], Siraev [20] and Kulesh [21].

In connection with the present work, bubbles coming from prebaked anodes were observed on industrial 150 kA cells. During anode change, the removal of butts gave free sight to the sides of two neighbouring anodes. Observations were made for ten cells. The observed bubble release frequencies were close to 1 Hz (0.94–1.19 Hz), which is within the range of published values (0.2–3 Hz). The size of the bubbles appeared to vary. Some large bubbles were observed, which caused large waves at the bath surface around the point of release (amplitude about 3–7 cm, as judged visually). Smaller bubbles produced waves with 1–3 cm amplitude. The bubble sizes and patterns seemed to be somewhat

different from cell to cell. In some cells, the middle part of the anode side was 'more active' (more bubbles released), but in other cases the outer part. Although the bubble release pattern was not regular, the release sites were approximately 20 cm apart in average. From these observations, the average bubble volume was estimated to be in the order of 100 ml.

Aaberg [19] studied gas volume and gas bubble layer characteristics. The experimental cell was a relatively large carbon crucible containing molten electrolyte. The bubble volume was measured indirectly by monitoring fluctuations in the bath level during electrolysis. It was found that the gas release pattern was consistent with the physical models, with most of the gas being evolved in discrete large bubbles. The release frequency was similar to the dominant frequency found in industrial cells.

The works cited above suggest that the gas layer at the anode is dominated by large, slab-like bubbles. It is likely, however, that there must be a number of smaller bubbles between the slabs, possibly residing at the anode during their formation and initial growth. Such small bubbles will be 'swallowed' by the larger slabs sweeping along the anode.

A review of data considering the geometry of the bubbles, as extracted from the literature, is presented in Table 1. Based on these estimations about the bubbles obtained mainly by physical modelling and measurements on industrial cells, it was decided to model five scenarios:

(i) Bubbles simulated as homogeneous layer with constant resistivity. The thickness of the layer was assumed to be 5 mm.

(ii) Large bubbles simulated as discrete slabs with width of 2.4–7.6 cm.

(iii) The same as item (ii), but with more realistic shape of the large slabs having a thick front and a thinner trailing part according to Fortin et al. [3], Solheim and Thonstad [17] and also in this work.

(iv) Combination of items (i) and (ii); small bubbles simulated as a homogeneous layer with constant resistivity and large bubbles simulated as discrete slabs.

(v) The same as item (iv), but with variable distribution of resistivity of bubble layer between the larger slabs. It was assumed that the resistivity increased linearly from the trailing edge of the leading slab to the leading edge of the trailing slab.

## 3. Description of the mathematical model

### 3.1. *Geometry and boundary conditions*

The geometry of the mathematical model was two-dimensional, as shown in Figure 3. The vertical 2D cross section represents a plane through the center of a prebaked anode in a 150 kA industrial cell having 20 anodes. The anode immersion depth was assumed to be 16.5 cm, and the interpolar distance was 4.5 cm (for
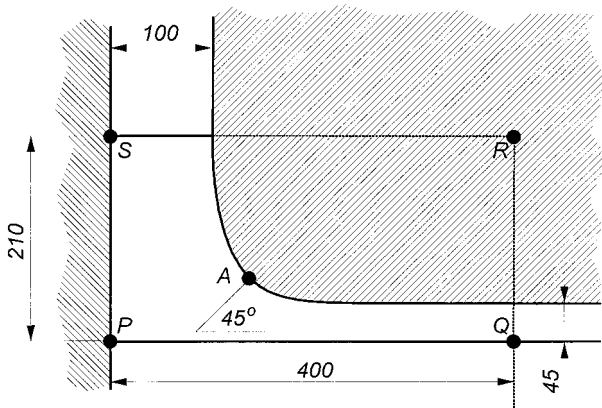
*Fig. 3.* Sketch showing the 2D model, comprising anode, sideledge, electrolyte, and aluminium. Calculation was performed within the rectangle QPRS. All dimensions are in mm.

other dimensions, see Figure 3). It was assumed that all anodes in the cell had the same current, and the average current density at the underside of the anode was taken to be 0.75 A cm$^{-2}$. In practice, the difference between the currents to each anode block is probably less than 20% [22].

The rounded-off shape of the anode was obtained on the basis of previous calculations and measurements [6, 22]. The results were verified using a probing technique [5, 23] and by measuring the shape of butts taken out of the cell [6, 22].

Variations in temperature and electrolyte composition influence the shape of the sideledge. Hence, the position of the intersection between electrolyte, aluminium and ledge (point P in Figure 3) may vary during electrolysis. The shape of the ledge, as well as the position of point P in Figure 3, influence the current distribution on the anode. However, if the distance between the sideledge and the side of the anode is more than 15 cm, the anode shape does not have significant influence on the anodic current densities [8].

The electrical field in the cell (within the rectangle PQRS in Figure 3) was calculated at steady state conditions. The Laplace equations (LE) in the selected 2D cross section were solved using the finite element method (FEM) with triangular elements (15 000–18 000 elements, 8000–9000 nodes (triangles with approximate length of the side of 2–3 mm)). To calculate current density (c.d.), the Laplace equation (LE) for the Galvani potential in 2D was solved. In the present, as well as in previous work [5–8] we used a mesh generator included in commercial software packages (Cosmos® and Patran®) and a solver developed by the authors [6].

### 3.2. Assumptions made for the solution of the Laplace equations

The LE in the chosen 2D cross sections was solved using the finite element method (FEM) with triangular elements. The following conditions, ((i)–(viii)), were applied:

(i) Secondary current distribution was considered on both anode and cathode. For the anodic activation overvoltage the following Tafel-type equation was applied [10],

$$\eta_A = 0.5 + 0.25 \log(j_A) \qquad (2)$$

where $j_A$ is in A cm$^{-2}$. The reversible cell voltage was taken to be 1.23 V [10, 1] (formally negative), referred to the aluminium cathode.

(ii) It was assumed that the line R – S in Figure 3 was equipotential, having a potential $U_{cell}$. The line R – S is about 10 cm underneath the anode yoke. 3D calculations of the thermoelectric field with the primary current distribution (in the entire 150 kA cell with 20 anodes) showed that the equipotential lines are parallel with the anode underside [22]. The contact potentials between the iron and the carbon material influenced the equipotential lines down to 10 cm underneath the yoke, whereas the equipotential lines were horizontal further down.

(iii) For the cathodic overvoltage linear polarization was assumed [10],

$$\eta_C = 0.08 j_C \qquad (3)$$

Both the cathodic current density and the cathodic overvoltage are formally negative.

(iv) The resistivity of the electrolyte was taken to be 0.5 Ω cm [24], except within the bubble layer when the bubbles were treated as a homogeneous dispersion.

(v) The resistivity of the anode was taken to be 0.005 Ω cm [10].

(vi) The calculations represent the conditions in the cell at a specific time, rather than being the average for a longer period. With the chosen method of computing having a fixed coordinate system with point P as origin, no net movement of the anode contour could be assumed. In reality, the cathode surface moves relative to a fixed point in the cell as the metal accumulates, and the position of the anode varies as well. The metal is being tapped (every day or every second day), whereby there is a sudden drop in the metal level, and the position of the anodes is lowered accordingly. Furthermore, due to variations in temperature and electrolyte composition, the shape and thickness of the sideledge varies in practice.

### 3.3. Assumptions made for the modelling of gas bubbles

#### 3.3.1. Bubbles treated as a homogenous layer with higher resistivity

In scenario 1 (see above) the bubbles were treated as a homogeneous layer with higher resistivity than the bubble-free electrolyte. The extra voltage drop due to the presence of bubbles ($\Delta U$) then becomes

$$\Delta U = j \delta_b (\rho_b - \rho_0) \qquad (4)$$

where $\delta_b$ is the thickness of the bubble layer (taken to be 5 mm) and $\rho_b$ and $\rho_0$ are the resistivities of the bubble layer and in the bubble-free electrolyte, respectively. $\rho_0$ was taken to be 0.5 $\Omega$ cm, whereas $\rho_b$ was varied up to 2.61 $\Omega$ cm. In this model, values of $\rho_b$ in the range 1–1.5 $\Omega$ cm give realistic extra voltage drops (in the range 0.2–0.4 V).

### 3.3.2. Bubbles treated as large discrete slabs

Based on the results obtained in physical models (also presented in Table 1) and our physical model, it appears that large bubbles can be approximated as discrete slabs. The effect of such bubbles on the bubble-induced extra voltage drop must be calculated numerically, since the electric field underneath the bubble layer will be affected. To estimate the effect of the geometry of such slabs, some preliminary calculations were performed (primary current distribution). The bubbles were assumed to be two-dimensional with thickness $h = 0.5$ cm, and the interpolar distance was $H = 4.5$ cm. The bubble length ($L_b$, see Figure 4) and the centre-centre distance between bubbles ($L_{CC}$) were varied. The numerical results could be approximated by the following equation,

$$\Delta U = \rho_0 j \cdot \left\{ \left( \frac{26.82\,\varphi^{1.75} - 21.96\,\varphi^{3.5}}{1 - \varphi} \right) \times \left( \frac{L_{CC}}{1 + 4.77\,L_{CC}^2} \right) + \frac{0.5\,\varphi}{1 - \varphi} \right\} \tag{5}$$

where $\varphi = L_b / L_{CC}$. At $L_{CC} = 15$ cm, extra ohmic voltage drops in the range 0.1–0.8 V can be calculated with bubble dimensions $L_b$ ranging from about 2.5 to 7.5 cm.

### 3.3.3. Smaller bubbles between large slabs

Smaller gas bubbles are probably formed between the larger slabs. Immediately behind the trailing edge of a gas slab the anode is gas-free, while the small bubbles are 'swallowed up' by the leading edge of the next slab. The volumetric rate of gas evolution ($q$) in the area between slabs is given by

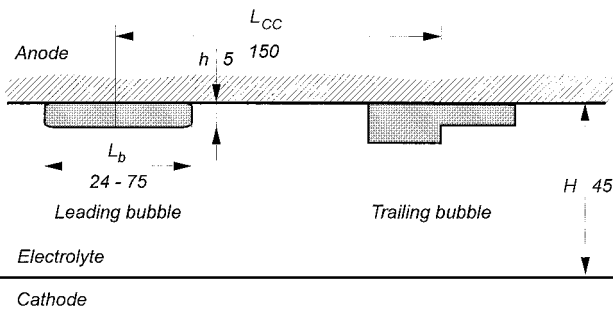$$q = \frac{j}{4F} \times \frac{RT}{P(1 - \varphi)} \tag{6}$$



Fig. 4. Sketch of two large bubbles simulated as large discrete slabs (with necessary dimensions in mm); right hand sided bubble is depicted with head-and-trail (dimensions of such bubbles were varied to see the influence on the current density). Also see Figure 1.

with the symbols, $F, R, P$ and $T$ having their usual meanings. By assuming that the smaller bubbles reside at their nucleation points, the average gas volume per unit area ($h'$) equals the product of the gas evolution rate and the time of growth. The maximum growth time (time between the tail of the leading slab and the head of the trailing slab) becomes

$$t_{max} = \frac{L_{CC}(1 - \varphi)}{u} \tag{7}$$

where $u$ is the velocity of the slabs. The maximum amount of gas (at the head of the trailing slab) then becomes

$$h'_{max} = \frac{j}{4F} \times \frac{RTL_{CC}}{Pu} \tag{8}$$

By inserting numerical values ($j = 7500$ A m$^{-2}$, $T = 1240$ K, $L_{CC} = 0.15$ m, $P = 1.04 \times 10^5$ Pa, $u = 0.3$ m s$^{-1}$) we obtain $h'_{max} = 0.0010$ m$^3$ m$^{-2}$. It is probable that such a layer of small bubbles contributes significantly to the total gas induced resistance. However, the size of the bubbles (or number of nucleation points per unit area), which is necessary to calculate the resistance, is not known. Therefore, the calculations in the present work was carried out in a similar manner as described in Section 3.3.1, assuming a linear relationship between the resistivity of the bubble layer and the position between larger gas slabs.

## 4. Results and discussion

To simplify the presentation of the results, the limit between the side and the underside of the anode was defined as shown in Figure 3. The side of the anode was defined as the part of the anode extending from the surface of the electrolyte to point A in Figure 3. The orthogonal projection at point A intercepts at an angle of 45° with the horizontal line representing the flat part of the anode. According to this definition, the underside of the anode begins at point A and covers the flat bottom part of the anode. In the Figures concerning anodic current density, the positions given start at the bath surface and follow the contour of the anode so that both the side and the underside of the anode are included in the same figures.

### 4.1. Scenario 1: Small bubbles treated as a homogeneous layer

Some results from the calculations are presented in Figure 5, which shows the current density at the underside of the anode (above point Q in Figure 3) as a function of the resistivity of the bubble layer. An extra voltage drop of 0.4 V due to the bubble layer corresponded to a decrease in the c.d. of 0.1 A cm$^{-2}$ (In practice, the cell voltage will be increased to compensate for the extra resistance).
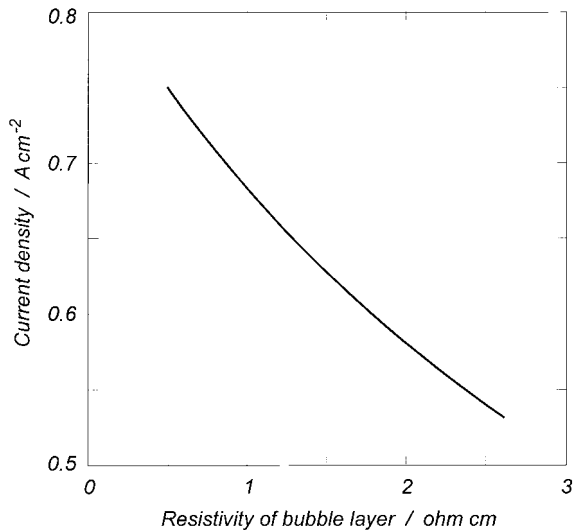
*Fig. 5.* Current density at the anode underside (near point Q in Figure 4) as a function of the resistivity of the bubble layer. Thickness of the bubble layer was 5 mm.

## 4.2. *Scenario 2: Large bubbles simulated as discrete slabs*

In this case, the bubbles were simulated as discrete slabs as shown in Figure 4. The slabs were positioned with 15 cm centre–centre distance, the thickness of the slab was 0.5 cm, and the dimension of the slab in the direction of motion was varied from 2.5 to 7.8 cm.

The anodic current densities are shown in Figure 6. Three regions with zero current density can be observed, corresponding to the position of the gas slabs. Close to the bubbles there appears to be local maxima in the current density. Those maxima are related to the potential field inside the anode. When a fraction of the anode surface is blocked, the potential above that area increases, causing horizontal currents within the anode
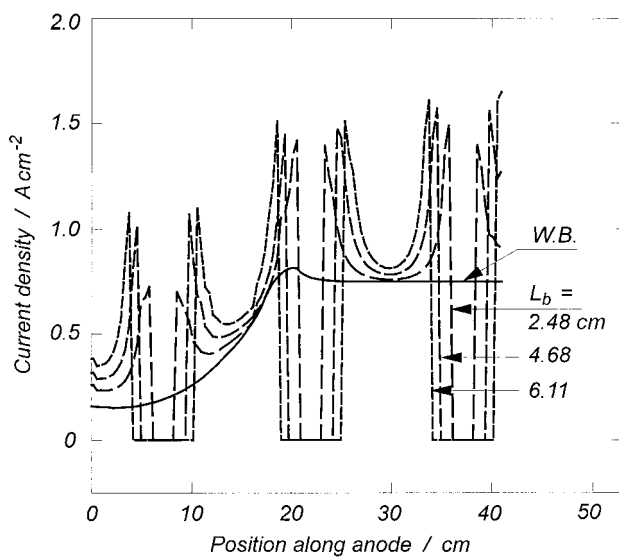
directed from the centre of the slab towards the edges. If the current and potential fields are modelled without taking the interior of the anode into consideration, such current maxima do not appear.

Figure 7 shows the cathodic current densities for the same simulations. Two local minima are present, which are positioned just underneath the second and third maxima in Figure 6. The bubble positioned on the side of the anode does not influence the cathodic current density significantly, because the current field is 'smeared out' due to the long distance between that bubble and the cathode.

## 4.3. *Scenario 3: Homogeneous layer of small bubbles with constant resistivity between discrete slabs*

As would be expected, the presence of small bubbles between the slabs brought about a decrease in the current densities between the large slabs. Some results are given in Figure 8, which shows the local current density at the point located in the middle between the two slabs at the horizontal part of the anode. Three curves are shown for different widths of the slabs. The uppermost point in each curve represents the absence of small bubbles (bubble layer with same resistance as the bulk of the electrolyte).

## 4.4. *Scenario 4: Large bubbles modelled with a thick front and a thinner trailing part*

In this case, the shape of the gas slabs were modified to have a shape similar to the large bubbles shown in Figure 2, by adding a front with thickness of 1–1.5 cm and length 5–10 cm (as sketched in Figure 4(b)). Other slab dimensions remained unchanged.

The decrease in the local anodic current densities, as compared to the slabs without a thicker front, was up to 7%. The cathodic current densities decreased for less
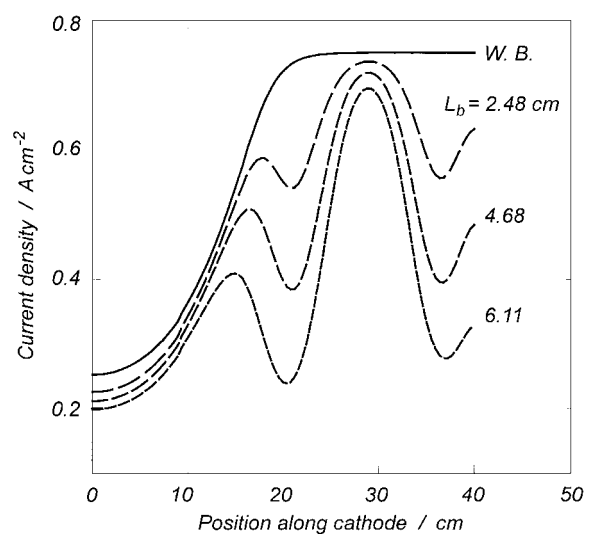


*Fig. 6.* Anodic current densities as a function of position (starting at bath surface and ending above point Q in Figure 3) at different values of the bubble dimension $L_b$ in Figure 4. W.B.: without bubbles present.



*Fig. 7.* Cathodic current densities as a function of position between point P and Q in Figure 3 at different values of the bubble dimension $L_b$ in Figure 4. W.B.: without bubbles present.
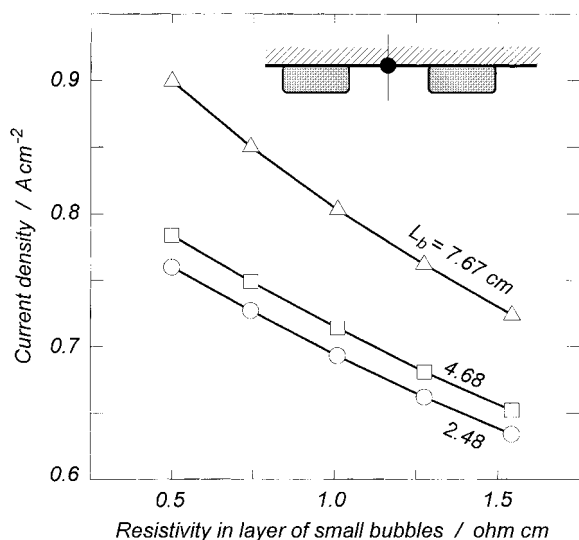
*Fig. 8.* Anodic current density at the middle between the two gas slabs located at underside of the anode as a function of the resistivity in the layer of small bubbles between the slabs. Results are shown for three slab dimensions.

than 3%. The local maxima and minima remained, and were attenuated for less than 3%. This means that the main effect of the larger gas slabs is due to the distortion of the current field underneath the bubble, whereas the partial restriction of the available area for passing of current between the bubbles is less important.

## 4.5. *Scenario 5: Influence of the layer of small bubbles between two successive larger bubbles*

In this case, it was assumed that the resistivity increased linearly from the trailing edge of the leading slab to the leading edge of the trailing slab. The influence of the layer of small bubbles on the anodic current densities was less than 3%, what confirms the conclusion from the previous Section.

## References

1. W.E. Haupin, *J. Metals* **23** (1971) 46–49.
2. R. Odegard, A. Solheim and K. Thovsen, *in* R. Cutschall (ed.), 'Light Metals 1992' (TMS, Warrendale, PA), pp. 457–463.
3. S. Fortin, M. Gerhardt and A.J. Gesing, *in* J.P. McGeer (ed.), 'Light Metals 1984' (TMS, Warrendale, PA), pp. 721–741.
4. F.N. Ngoya and J. Thonstad, *Electrochim. Acta* **30** (1985) 1659–1664.
5. J. Zoric, I. Rousar, J. Thonstad, Z. Kuang, *J. Appl. Electrochem.* **26** (1996) 795.
6. J. Zoric, I. Rousar and J. Thonstad, *J. Appl. Electrochem.* **27,** (1997) 916.
7. J. Zoric, I. Rousar, J. Thonstad and T. Haarberg, *J. Appl. Electrochem.* **27** (1997) 928.
8. J. Zoric, I. Rousar and J. Thonstad, *in* R. Huglen (ed.), 'Light Metals 1997' (TMS, Warrendale, PA), pp. 449–456.
9. G.J Houston, M.P. Taylor, D.J. Williams and K. Grjotheim, *in* L.G. Boxall (ed.), 'Light Metals 1988' (TMS, Warrendale, PA), p.643.
10. K. Grjotheim, H. Kvande, 'Introduction to Aluminium Electrolysis' (Aluminium-Verlag, Düsseldorf, 1993).
11. R.C. Dorward, *J. Appl. Electrochem.* **13** (1983) 569–575.
12. K. Grjotheim and B.J. Welch, 'Aluminium Smelter Technology', 2nd edn (Aluminium-Verlag, Düsseldorf, 1988).
13. S. Rolseth, A. Solheim and J. Thonstad, 'Gas Induced Waves at the Bath – Metal Interface in Hall – Heroult Cells', Proceedings of the International Symposium on Reduction and Casting of Aluminium (Aug. 1988), p. 229.
14. W.D. Zhang, 'Modelling of Anode Gas Evacuation and Current Efficiency in Hall – Heroult cells, PhD thesis, Dept. of Chemical and Materials Eng., University of Auckland (1993).
15. W.D. Zhang, et al. 'Modelling of Anode Gas Evolution in a Hall – Herroult Cell', CHEMECA Australasian Chemical Engineering Conference 91 (Newcastle, 18–20 Sept. 1991), pp. 721–727.
16. T.M. Hyde and B.J. Welch, *in* R. Huglen (ed.), 'Light Metals 1997' (TMS, Warrendale, PA), pp. 333–340.
17. A. Solheim and J. Thonstad, *in* R.E. Miller (ed.), 'Light Metals 1986' (TMS, Warrendale, PA), pp. 397–403.
18. W.E. Haupin, The 3rd International Course on the Process Metallurgy of Aluminium (Trondheim, Norway, 1984), chapter 7.
19. R.J. Aaberg, V. Ranum, K. Williamson and B.J. Welch, *in* R. Huglen (ed.), 'Light Metals 1997' (TMS, Warrendale, PA), p. 341.
20. N.S. Siraev, G.V. Forsblom and D. Ya. Khalpakchi, *Non-Ferrous Metals* **17**(7) (1976) 33–35.
21. K. Kulesh, A.A. Dimitrov and V.O. Volodchenko, *Non-Ferrous Metals*, **43**(9) (1970) 25.
22. J. Zoric, J. Thonstad and T. Haarberg, *in* B. Welch (ed.), 'Light Metals 1998' (TMS, Warrendale, PA), pp. 445–453.
23. Z. Kuang and J. Thonstad, *J. Appl. Electrochem.* **26** (1996) 481.
24. J. Hives, J. Thonstad, A. Sterten and P. Fellner, *in* B. Welch, (ed.), 'Light Metals 1998' (TMS, Warrendale, PA), pp. 187–194.
25. E. Dewing, *Can. Met. Quart.* **30** (1991) 153–161.
26. H. Oye, J. Xue, *in* J. Evans (ed.), 'Light Metals 1995' (TMS, Warrendale, PA), pp. 265–271.
27. A.I. Begunov and B.I. Ayushin, *Non-Ferrous Metals* **18**(6) (1975) 237–239.
28. A.I. Begunov, V.N. Kulkov, S.D. Tsymbalov and A.A. Silushkina, *Non-Ferrous Metals* **21**(6) (1978) 251–253.
29. A.I. Begunov, *Non-Ferrous Metals* **19**(1) (1976) 6–8.